DOI 10.24425/aee.2025.155962

Calculation of magnetostrictive vibration of four-node iron-core unit based on magnetic network method

HUIYING ZHANG[1,2]✉, JIABAO AN[1], MINGXING TIAN[1,2], SHENGJIE GU[1], SHOUHU HE[1], TIANGE WANG[1]

[1] *School of Automation & Electrical Engineering, Lanzhou Jiaotong University Lanzhou, CO 730070 China*

[2] *Rail Transit Electrical Automation Engineering Laboratory of Gansu Province Lanzhou Jiaotong University*

e-mail: ✉ *zhanghylz@163.com*

(Received: 21.07.2025, revised: 03.11.2025)

Abstract: At present, the analysis of iron core vibration often uses the finite element method, but its modeling process is complex and the calculation time is long. To address this issue, this paper proposes a magnetic mechanical coupled magnetostrictive vibration calculation model for iron cores based on the magnetic network method with four-node elements, intended to achieve fast and accurate vibration assessment. Taking the Epstein frame circle as the research object, a four-node element magneto-mechanical coupling model of the square circle was constructed. The calculation results were compared with the finite element simulation results at typical positions of the square circle, and the consistency of the magnetic flux density values and node displacements was good, verifying the effectiveness and accuracy of the proposed method. The comparison of simulation time shows that the four-node magneto-mechanical model significantly shortens the calculation time when calculating vibration displacement, providing new ideas and feasible methods for efficient calculation of iron core vibration and noise in electrical equipment.

Key words: fast calculation, four-node unit, grid synchronous discretization, magnetic network method, magneto-mechanical coupling, vibration displacement

1. Introduction

The iron core of electromagnetic equipment is inevitably subject to vibration during operation, and its vibration characteristics are the direct influencing factor of equipment noise. Research has shown that the vibration of electromagnetic equipment iron cores is mainly caused by the

magnetostriction of silicon steel sheets [1–3]. Although the magnetostriction deformation of a single silicon steel sheet is only a few micrometers per meter [4], due to the large size of the iron core in electromagnetic equipment in engineering practice, the displacement and vibration caused by magnetostriction cannot be ignored [5, 6]. Researchers have conducted research [7–9] on the vibration characteristics of laminated iron cores caused by magnetostriction. Traditional analysis of iron core vibration characteristics is often achieved using finite element software methods. References [10, 11] measured the anisotropic magnetostriction characteristics of non-oriented silicon steel sheets, obtained magnetostriction characteristics in different magnetization directions, and conducted finite element simulation calculations on the magnetostriction effect of a synchronous generator stator core. Reference [12] established a three-dimensional magneto-mechanical strong coupling model considering the magnetostriction effect of power transformer cores using the principle of energy variation, and calculated the magnetic field distribution and core vibration displacement of a three-phase three-column dry-type transformer using finite element analysis. Wataru Kitagawa [13] calculated the magnetostrictive force of each element, as well as the vibration displacement and noise caused by the magnetostrictive force, based on the finite element calculation of the element magnetic flux density.

The finite element method has the disadvantages of large computational complexity and long-time consumption [14], and its application to iron core vibration requires the establishment of a coupled model of electromagnetic equipment's electric, magnetic, and mechanical multiphysics fields. The multiphysics coupling model requires more complex numerical solution methods to handle, and different physical fields are discretized using different grids, which also require interpolation and reconstruction between grids. This increases the difficulty of solving the finite element method and often leads to long computation time and low efficiency, resulting in a decrease in computational efficiency.

In contrast, the Magnetic Resistance Network Analysis (RNA) [15–17] method significantly reduces computational complexity and analysis difficulty by constructing a magnetic circuit model while ensuring a certain level of accuracy. This method has high efficiency and good engineering applicability, and is suitable for most vibration characteristic analysis scenarios. Scholars have attempted to use RNA for vibration calculations. References [18, 19] established an equivalent magnetic network model for separable transformers based on the principle of equivalent flux tubes, and calculated the magnetic flux density of each unit through the constructed magnetic network model. Y. Hane, K. Nakamura [20] *et al*. calculated the magnetostriction force of a circular wound iron core using RNA and verified the effectiveness of the method by comparing it with the results obtained by the finite element method. However, they did not perform calculations related to vibration displacement. References [21, 22] derived the magnetostriction force of a three-node unit node based on energy functional theory and the magnetostriction force of a three-node triangular unit based on the principle of virtual work. The harmonic balance decomposition algorithm was applied to calculate the nonlinear magnetic field and displacement in the frequency domain. However, the three-node unit adopts a linear form function (first-order interpolation), and its displacement gradient remains constant within the unit, resulting in the strain field degrading to a constant strain state. Not only is it difficult to accurately describe the nonlinear strain distribution caused by the magnetostriction effect, but it also significantly reduces the calculation accuracy due to stress discontinuities between adjacent elements. In addition, although the three-node element is suitable for unstructured grids in geometrically complex areas, electromagnetic equipment (such as transformer cores) in power systems generally have regular geometric boundaries, which are more suitable for structured grid meshing with four-node elements.

In summary, this article proposes a magnetic mechanical coupling modeling method based on four-node magnetic network units. This method accurately describes the nonlinear strain distribution and achieves efficient calculation of iron core vibration through the coordinated discretization of the magnetic field force field, providing an effective way for rapid evaluation of electromagnetic equipment vibration and noise.

2. Methods and models

2.1. Equivalent magnetic network model

The core idea of the equivalent magnetic network model is that according to the magnetisation characteristics of the magnetic medium and the distribution characteristics of the magnetic field, the entire magnetic field domain space is discretely dissected into a number of simple and regular shaped units such as the square shown in Fig. 1(a), but also other shapes such as cylinders, rectangles, and fan rings. Each unit is equivalent to a magnetic circuit, and each unit is connected by nodes to form an equivalent magnetic network. Based on the similarity between the magnetic network and the electric network, the magnetic potential of each node point is obtained by the node

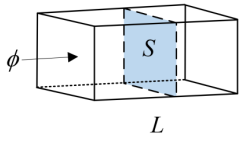

(a) Equivalent magnetic flux tube

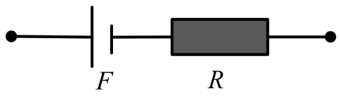

(b) Magneto-dynamic potential source

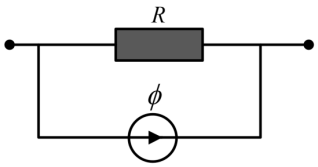

(c) Flux source

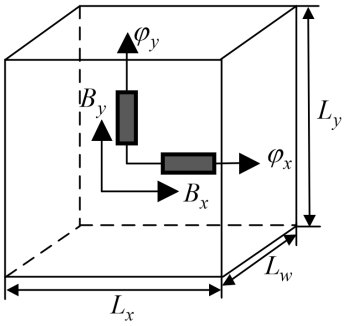

(d) Schematic diagram of flux tube flow direction

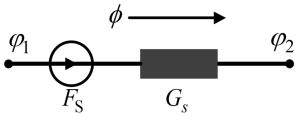

(e) A magnetically guided branch

Fig. 1. Equivalent magnetic network components

method or loop method, and then the relevant parameters of the magnetic field (such as magnetic flux, magnetic flux density and magnetic field strength). Equivalent magnetic network model is generally used to establish the flux tube method, each unit of the magnetic network as a flux tube, flux tube end surface for the equipotential surface, flux tube inside only longitudinal (perpendicular to the cross-section) and uniform magnetic flux, and isotropic and uniform magnetic medium, as shown in Fig. 1(a), it is the equivalent magnetic permeability calculation formula.

$$G = \frac{\mu S}{L}, \tag{1}$$

where S denotes the cross-sectional area of the flux tube perpendicular to the flux path, and L is the length of the flux path of the flux tube. The selection of different magnetisation curves for the calculation of magnetic permeability $\mu = B/H$ in the above equation will directly affect the accuracy of the magnetic field calculation. At present, the basic magnetisation curve describing the magnetisation of the core is widely used.

Another essential component in the equivalent magnetic network model is the excitation source, which is mainly a magnetokinetic potential source or a flux source, and the two excitation sources can be converted to each other, and the series connection of the magnetokinetic potential source F and the magnetoresistance R can be equated to a flux source and a magnetoresistance in parallel, as shown in Fig. 2(b) and Fig. 2(c), with the excitation source $\Phi_s = F/R = GF$.

Figure 2(a) shows the grid dissection unit, length L_x, width L_w, and height L_y; the flux tube in the dissection unit is a x, y two-dimensional structure, its flux flow is also in the x, y direction, and its x, y direction magnetic permeability calculation formula is shown in Eq. (2).

$$\begin{cases} G_X = \dfrac{\mu S}{L} = \dfrac{\mu(L_y L_w)}{L_x} \\ G_Y = \dfrac{\mu S}{L} = \dfrac{\mu(L_x L_w)}{L_y} \end{cases}. \tag{2}$$

The division unit is dissected according to Fig. 1(d), the magnetic network model is constructed, and the nodal method is used to write the nodal magnetic potential equation, and the magnetic permeability matrix G in the nodal magnetic potential equation contains a large number of zero elements, which belongs to the higher-order sparse matrix, so it should be solved by the Gauss–Seidel iteration method.

Figure 1(e) shows any one of the magnetic network models of the magnetic conduction branch, assuming that its two ends of the magnetic potential are φ_1, and φ_2. F_{s1} is the magnetic momentum of the branch, then the branch magnetic field parameters can be calculated through Formula (3).

$$\begin{cases} \Phi = G(\varphi_1 - \varphi_2 - F_S) \\ B = \dfrac{\Phi}{S} \\ H = \dfrac{B}{H} \end{cases}, \tag{3}$$

where G is the magnetic permeability of the branch, S is the average cross-sectional area of the magnetic permeability, and L is the length of the magnetic circuit.

2.2. Basic structure of the 25 cm Epstein frame

The 25 cm Epstein frame (hereinafter referred to as the square coil) consists of four primary coils, four secondary coils and a specimen as the core. The four coils of the primary and secondary windings are connected in series, and the strips constituting the specimen are inserted therein, with a structure similar to an unloaded transformer. The structure is shown in Fig. 2(a). The square coil core grid dissection is given in Fig. 2(b).

2.3. Magnetic network model of Epstein frame

This paper establishes the equivalent magnetic network model of the Epstein frame considering the core saturation nonlinearity and magnetic leakage, divides the Epstein frame into units according to Fig. 2(b), and replaces each divided unit equivalently according to the flux tube flux flow schematic shown in Fig. 2(a), and establishes its two-dimensional equivalent magnetic network model by using the nodal method to obtain the equivalent magnetic network model shown in Fig. 2(c).

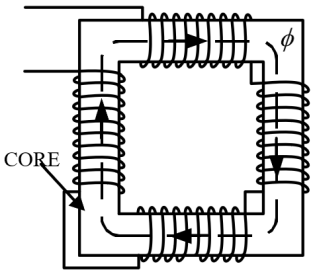

(a) Structure of Epstein frame

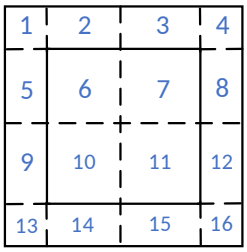

(b) Magnetic network grid

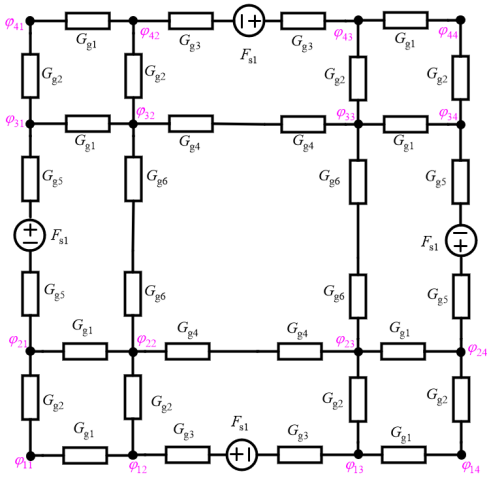

(c) Epstein frame and its magnetic network mesh division

Fig. 2. The equivalent magnetic network model of Epstein frame

The equivalent magnetic network model in Fig. 2(c) consists of two units with different properties, the equivalent magnetic permeability and the equivalent magnetic potential, and the equivalent magnetic permeability is divided into linear magnetic permeability and nonlinear magnetic permeability.

1. Linear permeability: G_{g4}, G_{g6}, the size of their permeability is independent of the magnitude of the magnetic flux passing through them, and is only determined by the structural dimensions of the square ring, which is calculated as follows:

$$\begin{cases} G_{g4} = \dfrac{\mu_0 S}{L_x} \\ G_{g6} = \dfrac{\mu_0 S}{L_y} \end{cases}, \tag{4}$$

   where μ_0 is the air permeability, L is half the length of the inner circle of the square ring, and S is the cross-sectional area of the square ring.
2. Non-linear permeability: $G_{g1}, G_{g3}, G_{g2}, G_{g5}, G_{c1}, G_{c2}$, the size of their permeability is not only related to the size of the Epstein frame structure but also related to the degree of magnetic saturation of the iron core, which is calculated as follows:

$$\begin{cases} G_{gm} = \dfrac{\mu S}{L_x} \\ G_{gn} = \dfrac{\mu S}{L_y} \end{cases}, \quad (m = 1, 3,\ n = 2, 5) \quad \begin{cases} G_{c1} = \dfrac{\mu S}{\sqrt{2} L_x} \\ G_{c2} = \dfrac{\mu S}{\sqrt{2} L_y} \end{cases}, \tag{5}$$

   where L is the length of the magnetic circuit of the dissecting unit, and S is the cross-sectional area of the Epstein frame, $\mu = B/H$ is the core permeability, whose value can be calculated by interpolation according to the selected core magnetisation curve. This article selects the measured single-value *B–H* curve to characterize the magnetization characteristics of the iron core. To improve the accuracy of magnetic flux tube parameter calculation more effectively, combined with the measured magnetization curve data presented in Fig. 8, this paper uses segmented interpolation to establish a *B–H* curve model suitable for 30Q130, and its expression is as follows.

$$B = \mu_1 H + \sum_{i=2}^{k} (\mu_i - \mu_{i-1})(H - H_{i-1})\theta(H - H_{i-1}).$$

   In the equation, $\mu_i = \dfrac{B_i - B_{i-1}}{H_i - H_{i-1}}$ denotes the slope of the *B–H* curve within each segmented interval; k represents the number of fitting segments, while $\theta(H - H_i)$ signifies the unit step function.
3. Equivalent magnetic potential calculation equation

$$F_{S1} = NI, \tag{6}$$

   where N is the number of winding turns and I is the winding side current.

According to the similarity of electric and magnetic networks, either the loop method or the nodal method can be used to write the magnetic network equations, because the nodal method can be easily extended to large-scale mathematical equations, allowing simple and convenient solutions to be established. The advantage of this work is the adoption of the nodal method and, according to the corresponding node numbering, the establishment of the nodal magnetic potential equation.

$$G\varphi = \Phi_S, \tag{7}$$

i.e.

$$\begin{bmatrix} G_{11} & G_{12} & 0 & 0 \\ G_{21} & G_{22} & G_{23} & 0 \\ 0 & G_{32} & G_{33} & G_{34} \\ 0 & 0 & G_{43} & G_{44} \end{bmatrix} \begin{bmatrix} \varphi_1 \\ \varphi_2 \\ \varphi_3 \\ \varphi_4 \end{bmatrix} = \begin{bmatrix} \Phi_{S1} \\ \Phi_{S2} \\ \Phi_{S3} \\ \Phi_{S4} \end{bmatrix}, \tag{8}$$

where G is the magnetic permeability matrix, φ is the magnetic potential vector, and Φ_S is the flux source vector.

The submatrices of the magnetic permeability matrix G

$$G_{11} = \begin{bmatrix} G_{g1}+G_{g2} & -G_{g1} & 0 & 0 \\ -G_{g1} & G_{g1}+G_{g2}+\frac{1}{2}G_3 & -\frac{1}{2}G_{g3} & 0 \\ 0 & -\frac{1}{2}G_3 & G_{g1}+G_{g2}+\frac{1}{2}G_{g3} & -G_{g2} \\ 0 & 0 & -G_{g2} & G_{g1}+G_{g2} \end{bmatrix},$$

$$G_{12} = G_{21} = \operatorname{diag}\left(-G_{g2} \;\; -G_{g2} \;\; -G_{g2} \;\; -G_{g2}\right),$$

$$G_{22} = \begin{bmatrix} \frac{1}{2}G_5+G_{g1}+G_{g2} & -G_{g1} & 0 & 0 \\ -G_{g1} & G_{g1}+G_{g2}+\frac{1}{2}G_4+\frac{1}{2}G_{g6} & -\frac{1}{2}G_{g4} & 0 \\ 0 & -\frac{1}{2}G_4 & G_{g1}+G_{g2}+\frac{1}{2}G_{g4}+\frac{1}{2}G_{g6} & -G_{g1} \\ 0 & 0 & -G_{g1} & \frac{1}{2}G_{g5}+G_{g1}+G_{g2} \end{bmatrix},$$

$$G_{23} = G_{32} = \operatorname{diag}\left(-\frac{1}{2}G_{g5} \;\; -\frac{1}{2}G_{g6} \;\; \frac{1}{2}G_{g6} \;\; -\frac{1}{2}G_{g5} \right),$$

$$G_{33} = G_{22}, \quad G_{34} = G_{43} = G_{12}, \quad G_{44} = G_{11}.$$

Components of the magnetic potential vector φ

$$\varphi_q = \left[\varphi_{q1} \;\; \varphi_{q2} \;\; \varphi_{q3} \;\; \varphi_{q4} \right]^T, \quad (q = 1, 2, 3, 4).$$

Flux source vector Φ_S individual component vectors

$$\Phi_{s1} = \left[\Phi_{s11} \;\; \Phi_{s12} \;\; \Phi_{s13} \;\; \Phi_{s14} \right]^T = \left[0 \;\; G_{g3}F_{S1} \;\; -G_{g3}F_{S1} \;\; 0 \right]^T,$$

$$\Phi_{s2} = \left[\begin{array}{cccc}\Phi_{s21} & \Phi_{s22} & \Phi_{s23} & \Phi_{s24}\end{array}\right]^T = \left[\begin{array}{cccc}-G_{g5}F_{S1} & 0 & 0 & 0\end{array}\right]^T,$$

$$\Phi_{s3} = \left[\begin{array}{cccc}\Phi_{s31} & \Phi_{s32} & \Phi_{s33} & \Phi_{s34}\end{array}\right]^T = \left[\begin{array}{cccc}0 & -G_{g3}F_{S1} & G_{g3}F_{S1} & 0\end{array}\right]^T,$$

$$\Phi_{s4} = \left[\begin{array}{cccc}\Phi_{s41} & \Phi_{s42} & \Phi_{s43} & \Phi_{s44}\end{array}\right]^T = \left[\begin{array}{cccc}0 & -G_{g3}F_{S1} & G_{g3}F_{S1} & 0\end{array}\right]^T.$$

The magnetic flux density is obtained by solving the constructed square-loop magnetic network model, and the solved flux density is used as the excitation to calculate the magnetostrictive force, which is then substituted into the vibration system equation to solve the magnetostrictive displacement.

2.4. Basic equations of mechanics

The discretization mode is adopted for the iron core silicon steel sheet instead of the original continuous body, but within each unit, it is considered to comply with the basic assumptions of elastic mechanics.

The stress-strain relationship can be written in matrix form as Eq. (9).

$$\{\sigma\} = [D]\{\varepsilon\}, \tag{9}$$

where D is called the elasticity matrix and is determined by the modulus of elasticity E and Poisson's ratio θ. Under the action of external force or stress, the elastomer will produce displacement and deformation, and the displacement of any point can be expressed by the displacement components uv and w along the three directions of the right-angle coordinate axis. In the study of the vibration problem of stacked cores, the deformation of the magnetic domains of the silicon steel sheet is mainly in the xy direction, and the change in the square z upward can be ignored compared to the xy direction [19], so the vibration of the stacked cores is approximated and simplified as a planar problem.

2.5. Calculation of unit magnetostrictive force

The magnetostriction force can be calculated based on the principle of virtual work. According to the principle of virtual work, the virtual work done by the node force on virtual displacement is equal to the virtual work done by the stress on virtual strain, and the calculation formula for the equivalent magnetostriction force of the unit can be obtained.

$$F_s^e = K^e X_s = K^e(r\varepsilon_s^e). \tag{10}$$

Among them, K^e and ε_s^e, respectively, represent the stiffness matrix and magnetostrictive strain of the element, while r refers to the distance between the center of the element and the node of the element. The block matrix expression for the stiffness matrix of the four-node unit is shown in Eq. (11).

$$[K]^e = \left[\begin{array}{cccc}\left[K_{11}^e\right] & \left[K_{12}^e\right] & \left[K_{13}^e\right] & \left[K_{14}^e\right] \\ \left[K_{21}^e\right] & \left[K_{22}^e\right] & \left[K_{23}^e\right] & \left[K_{24}^e\right] \\ \left[K_{31}^e\right] & \left[K_{32}^e\right] & \left[K_{33}^e\right] & \left[K_{34}^e\right] \\ \left[K_{41}^e\right] & \left[K_{42}^e\right] & \left[K_{43}^e\right] & \left[K_{44}^e\right]\end{array}\right], \tag{11}$$

where the sub-matrix expression for K^e is given in the following equation.

$$\left[K_{rs}^e\right] = \begin{bmatrix} K_{rs}^{11} & K_{rs}^{12} \\ K_{rs}^{21} & K_{rs}^{22} \end{bmatrix} = \frac{Ehab}{4(1-\theta^2)^2} \times$$

$$\begin{bmatrix} \frac{1}{x_r x_s}\left(1+\frac{b^2}{3y_r y_s}\right)+\frac{1-2\theta}{2(1-\theta)y_r y_s}\left(1+\frac{a^2}{3x_r x_s}\right) & \frac{\theta}{(1-\theta)y_s x_r}+\frac{1-2\theta}{2(1-\theta)x_s y_r} \\ \frac{\theta}{(1-\theta)x_s y_r}+\frac{1-2\theta}{2(1-\theta)y_s x_r} & \frac{1}{y_r y_s}\left(1+\frac{a^2}{3x_r x_s}\right)+\frac{1-2\theta}{2(1-\theta)x_r x_s}\left(1+\frac{b^2}{3y_r y_s}\right) \end{bmatrix},$$

$$(rs = 1, 2, 3, 4),$$

where E is Young's modulus, h is the thickness of the silicon steel sheet, and a, b are the half-length and half-width of the quadrilateral unit, respectively.

2.6. Transfer of magnetostrictive force to nodal force

The element magnetic flux density is regarded as distributed in the center of the element. According to the assumption of the finite element, the force acting on the node must be the node load. Therefore, the element force needs to be converted into the node force according to the principle of static equivalence. The calculation expression of the node force of the four-node element mainly includes three steps. The detailed derivation process is as follows.

The first step is to determine the relationship between the displacement mode of the four-node element and the shape function to determine the element virtual displacement. As shown in Fig. 3, let the four-node rectangular element be subjected to a uniformly distributed physical force $F_V = [X\ Y]^T$ (where X, Y are the force of F in the direction of x and y), and the equivalent nodal load array obtained after the transfer to the node.

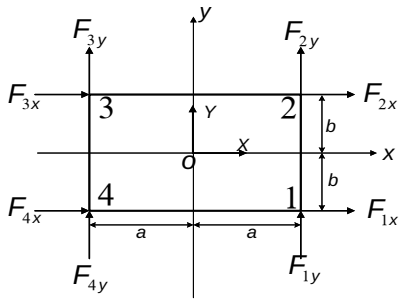

Fig. 3. Quadrilateral rectangular unit

$$\{F\}^e = \left[\ F_{1x}^e\ \ F_{1y}^e\ \ F_{2x}^e\ \ F_{2y}^e\ \ F_{3x}^e\ \ F_{3y}^e\ \ F_{4x}^e\ \ F_{4y}^e\ \right]^T.$$

Suppose that some kind of virtual displacement occurs in the unit shown in Fig. 7. At this time, the virtual displacement of the unit node is

$$\{\delta\Delta\}^e = \left[\ \delta u_1\ \ \delta v_1\ \ \delta u_2\ \ \delta u_2\ \ \delta u_3\ \ \delta u_3\ \ \delta u_4\ \ \delta u_4\ \right]^T.$$

According to the relationship between the displacement mode and the shape function of the four-node element [12], the virtual displacement in the element is

$$\{\delta f\}^e = [N]\{\delta\Delta\}^e, \tag{12}$$

where δf is the unit displacement function, N is the morphology function matrix, and $\delta\Delta$ is the imaginary displacement. In the second step, according to the principle of static equivalence and only considering the action of uniform body force, the unit load is transferred to four nodes 1, 2, 3, 4, and the general expression of the node force of the four-node rectangular element is obtained. According to the principle of static equivalence, that is, the load acting on the element is equal to the load transferred to the node, and their virtual work on any virtual displacement of the element is equal. When only the distributed body force $\{F_V\}$ is considered, the following formula is established.

$$(\{\delta\Delta\}^e)^T\{F\}^e = \iint_A (\{\delta f\}^e)^T\{F_V\}^e h\mathrm{d}x\mathrm{d}y. \tag{13}$$

Substituting Eq. (12) into Eq. (13), and since $([\delta\Delta]^e)^T$ is arbitrary, we can obtain

$$\{F\}^e = \iint_A [N]^T\{F_V\}h\mathrm{d}x\mathrm{d}y, \tag{14}$$

where the integration is carried out on the area element A and the body force is evenly distributed on each subdivision element, then Eq. (14) can be written as

$$\{F\}^e = h\iint_A \begin{bmatrix} IN_1 & IN_2 & IN_3 & IN_4 \end{bmatrix}^T \mathrm{d}x\mathrm{d}y\{F\}. \tag{15}$$

In the formula, $N_1N_2N_3N_4$ are integrated respectively, and the integral result is substituted into Formula (15) to obtain Formula (16).

$$\{F\}^e = \left[F_{1x}^e, F_{1y}^e, F_{2x}^e, F_{2y}^e, F_{3x}^e, F_{3y}^e, F_{4x}^e, F_{4y}^e\right]^T = \frac{1}{4}\times 4abh\,[X\ Y\ X\ Y\ X\ Y\ X\ Y]^T. \tag{16}$$

Equation (16) is the general expression of the nodal force of a four-node rectangular element.

In the third step, the magnetostrictive force calculation formula is substituted into the general expression of the four-node force to obtain the calculation formula of the magnetostrictive force at each node of the four-node rectangular element. Substituting the magnetostrictive force F_s^e in the direction of x and y calculated by Eq. (10) into the general expression of node force (16), the equivalent node load matrix obtained by transferring the magnetostrictive force of the four-node rectangular element to the node can be obtained as Eq. (17).

$$\begin{aligned}\{F_s\}^e &= \left[F_{s1x}^e, F_{s1y}^e, F_{s2x}^e, F_{s2y}^e, F_{s3x}^e, F_{s3y}^e, F_{s4x}^e, F_{s4y}^e\right]^T \\ &= \frac{1}{4}\times 4abh\left[F_{sx}^e, F_{sy}^e, F_{sx}^e, F_{sy}^e, F_{sx}^e, F_{sy}^e, F_{sx}^e, F_{sy}^e\right]^T.\end{aligned} \tag{17}$$

In the formula, F_s^e is the unit magnetostrictive force, and $F_{sx}^e F_{sy}^e$ are the components of the unit magnetostrictive force in the direction of xy. The specific expression is

$$\{F_{s\Theta}\}^e = abh \begin{bmatrix} F_{sx}^e \\ F_{sx}^e \end{bmatrix} = abhK_{gm}^e \begin{bmatrix} r_{gx}\lambda_x \\ r_{gy}\lambda_y \end{bmatrix}, \quad (g = 1, 2, 3, 4; \quad m = 1, 2, 3, 4), \tag{18}$$

where h is the thickness of the silicon steel sheet unit; and r_{gx}, r_{gy} are the distances from the g node to the centre of the unit in the xy direction, respectively.

λ_x and λ_y represent the magnetostriction of the unit in the xy direction, respectively, and are obtained by interpolating the magnetostriction characteristic curve from the unit's magnetic induction strength B. Through the above analysis, the unit stiffness matrix of each subdivision unit is assembled to obtain the overall stiffness matrix, and the node force of each node of each unit is superimposed to obtain K and F in Formula (10). Then, the boundary conditions are applied to fix the lower element nodes of units 1, 8, 9 and 16 in Fig. 10, that is, the displacement of the four nodes is zero to simulate the actual transformer bottom fixed on the ground. Ferromagnetic materials are composed of many small magnetic domains. In general, magnetostriction will lead to the extension of magnetic domains in the direction of magnetic flux and the contraction of magnetic domains in the transverse direction, which makes the volume change. Therefore, the direction of the node force must be determined. It is assumed that the stretching force is applied to the component along the direction of the magnetic flux, and the contraction force is applied horizontally.

1. When the magnetic flux flows along the x direction, as shown in Fig. 4(a), the nodes 1, 2, 3, 4 along the direction of the magnetic flux are the stretching force in the x direction, and the vertical direction of the magnetic flux is the contraction force in the x direction.
2. When the magnetic flux flows along the y direction, as shown in Fig. 4(b), the nodes 1, 2, 3, 4 along the direction of the magnetic flux are the stretching force in the y direction, and the vertical direction of the magnetic flux is the contraction force in the x direction.
3. When the magnetic flux flows along the diagonal direction of the unit, as shown in Fig. 4(c), that is, nodes 2 and 4 are extension forces, and nodes 1 and 3 are contraction forces.

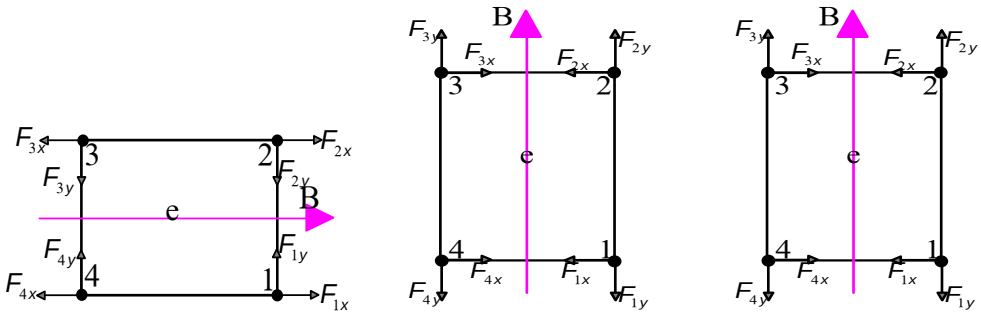

Fig. 4. Determination of the direction of node force

Figure 5 is a schematic diagram of the nodal forces of the four-node unit in the plane of the square coil iron core.

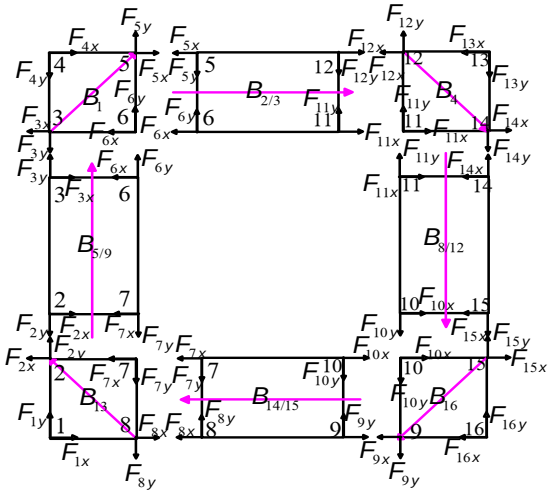

Fig. 5. Schematic diagram of node force in Epstein frame

2.7. Magnetostrictive vibration displacement calculation

Figure 6 provides detailed steps and calculation process for calculating the vibration displacement of the iron core based on the four-node magnetic network method.

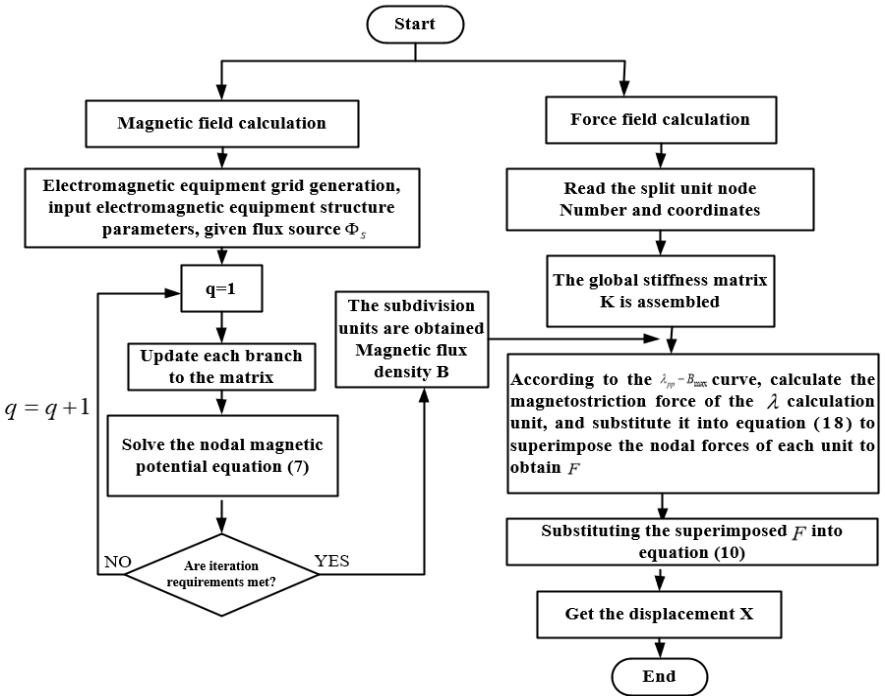

Fig. 6. Flowchart of the magnetic network method for calculating vibration displacement

For the core of electromagnetic equipment, the vibration differential equation of the system considering the magnetostrictive effect of silicon steel sheet is considered.

$$\boldsymbol{M}\frac{\partial^2 X}{\partial t^2} + \boldsymbol{R}\frac{\partial X}{\partial t} + \boldsymbol{K}X, \tag{19}$$

where $\boldsymbol{M}$ is the mass matrix, $\boldsymbol{R}$ is the damping matrix, $\boldsymbol{K}$ is the stiffness matrix, and F is the magnetostrictive force. The vibration frequency of the core of the electromagnetic equipment is generally low or quasi-static. When the vibration frequency is low, the vibration acceleration is small, the corresponding inertial force is small, and the inertial term can be ignored. Since the core vibration is a low-damping system, the damping term can also be ignored in quasi-static analysis. In summary, in the analysis of quasi-static low-damping systems, the dynamic effects (mass and damping) of the system can be ignored, and the system vibration differential Eq. (19) is simplified to the form of Eq. (20).

$$\boldsymbol{K}X = F. \tag{20}$$

3. Validation of the model

This article uses the Epstein frame coil magnetic measurement device to measure the basic magnetization curve of its iron-core material, as shown in Fig. 7(a), with the MATS-2010SD soft magnetic DC measurement device. A finite element model of a 25 cm Epstein frame coil was built using COMSOL finite element simulation (FEM) software, as shown in Fig. 7(b). The total number of turns of the winding is 700, the number of layers of the silicon steel sheets is 9, the length of each side silicon steel sheet is 280 mm, the thickness of each silicon steel sheet is 0.03 mm, and the selected silicon steel sheet material is 30Q130. Figure 8 shows the measured magnetization curve of 30Q130. This article selects four nodes located at different positions a, b, c, and d in the corner area of Figure 9 for calculation and comparative analysis. Figure 9 also provides the dimensions of Epstein's square circle.

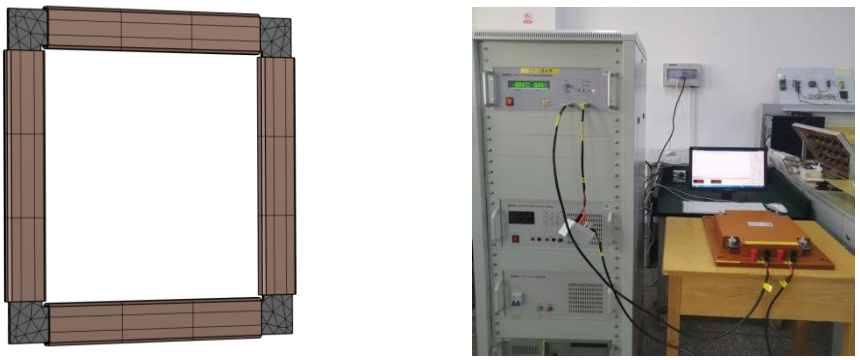

(a) Magnetic material measuring device (b) Finite element simulation model of square ring

Fig. 7. Magnetic measurement device and finite element model

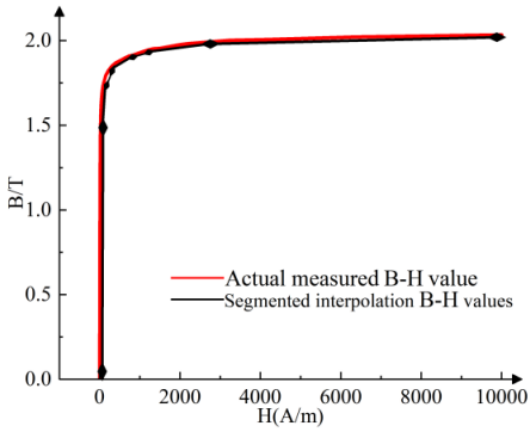

Fig. 8. Basic magnetization curve of 30Q130

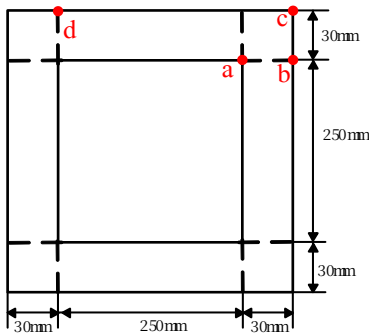

Fig. 9. Node position diagram

According to the calculation steps and methods of the magnetic mechanical coupling model based on the magnetic network method shown in Fig. 6, the magnetic field parameters and vibration displacement of the four nodes *a*, *b*, *c*, and *d* of the Epstein frame are calculated and analysed.

3.1. Comparative analysis of magnetic field calculations

Due to the symmetry of the Epstein frame ring structure, the magnetic flux density is uniformly distributed in the four sides. However, the different paths taken by the magnetic flux in the corner area result in an uneven distribution of magnetic flux density. Figure 10(a) shows a comparison of the *x*-direction and *y*-direction magnetic flux density waveforms at position *a* when the sinusoidal current excitation amplitude is 25 A. From the figure, it can be seen that the calculated results of the magnetic network model are basically consistent with the COMSOL simulation results in terms of waveform and amplitude.

Figure 10(b) gives the waveform of the magnetic flux density in the *x*-direction and *y*-direction at position *c* when the amplitude of the sinusoidal current excitation is 25 A. It can be seen from the figure that the finite element simulation result at position *c* is 0.0015 T, while the RNA calculation result is 0. The result is reasonable because electromagnetic devices such as the Epstein frame are passing along the shortest path when they pass through magnetically in the corner region, and the actual route of the flux in the corner region is an arc. The RNA calculation simplifies the magnetic density at point *c* to 0 by analysis, and the simplified result is also reasonable, as can be known from the COMSOL simulation result in Fig. 7(b). In this paper, the COMSOL simulation value is taken as the base value, and Eq. (21) is used to calculate the deviation of the RNA simulation result from the FEM.

$$\text{Relative error} = \frac{\text{RNA calculation value} - \text{COMSOL simulation value}}{\text{COMSOL simulation value}} * 100\%. \qquad (21)$$

Table 1 shows the comparison of magnetic flux density peaks at different locations under the same current excitation of 25 A. The relative error of magnetic flux density (*x*-direction and *y*-direction) at different detection points under the same current excitation is less than 8%.

Table 1. Comparison of peak magnetic flux density at different locations under 25 A same current excitation

Monitoring point number	RNA calculated value/T		FEM simulation value/T		Relative error/%	
	x-direction	*y*-direction	*x*-direction	*y*-direction	*x*-direction	*y*-direction
a	1.292	1.293	1.234	1.224	+4.71	+5.64
b	1.617	1.617	0.012	1.522	–100	+6.24
c	0	0	0.001	0.001	–100	–100
d	1.455	0	1.384	0.008	+5.13	–100

3.2. Comparative analysis of vibration displacement calculation

To grasp the distribution law of the vibration characteristics of the iron core, this article studies the distribution characteristics of vibration displacement by calculating the vibration displacement in different regions. By setting different excitation parameter values, study the magnitude and characteristics of vibration displacement under different excitations.

Figure 10(c) shows a comparison of the vibration displacement waveforms in the x and y directions at position a under a current excitation of 25 A. From the graph, it can be seen that the peak error between the calculated displacement value and the actual value is not significant, and the waveform and amplitude are basically consistent. However, the calculated value is slightly larger than the measured value, mainly because the influence of clamping force and sliding friction between the laminates was not considered during the calculation.

Figure 10(d) shows a comparison of peak-to-peak vibration displacement at different points under the same current excitation, and the calculated values are consistent with the simulated values. The comparison results between Fig. 10(b) and Fig. 10(c) verify the effectiveness of the magnetic network method in calculating magnetic flux density and vibration displacement. The results obtained from different positions are representative and can be analyzed in detail.

Figure 10(e) shows the a, b, d displacement vibration peak-to-peak value against the current trend, it can be seen that with the increase in current excitation, the displacement peak-to-peak value is also increasing, when the current amplitude < 35 A when the x, y-direction magnetic flux density $B < 1.434$ T, when the displacement basically shows a linear growth; however, with the increase in excitation current of the silicon steel sheet gradually reaches a saturated state, the displacement growth slows down and shows a nonlinear growth. Taking point a as an example, the displacement at 35 A is about twice that at 15 A. It can be seen in a certain range of current that the larger core vibration is more intense. Calculated data show that the displacement in the y-direction is about twice the displacement in the x-direction, and the vibration displacements in a and c are larger than those in b and d. The displacement in the y-direction is about twice the displacement in the x-direction.

Comparing the vibration displacements of points a and point c, as shown in Fig. 10(f), it can be concluded that the displacement values at point a are larger than those at point c. Analysis suggests that this may be due to the uneven distribution of magnetic flux density along the path of magnetic flux passing through the corners of the iron core, resulting in significant magnetostriction and stronger vibrations. Therefore, in order to alleviate this phenomenon, when designing electromagnetic devices with corners, the corners should be treated accordingly.

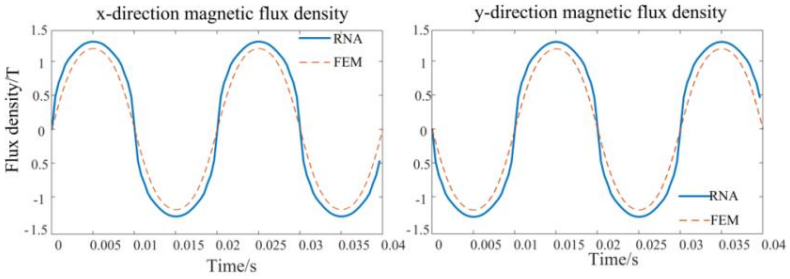

x-direction *y*-direction

(a) Position *a* magnetic flux density waveform at 25 A excitation source

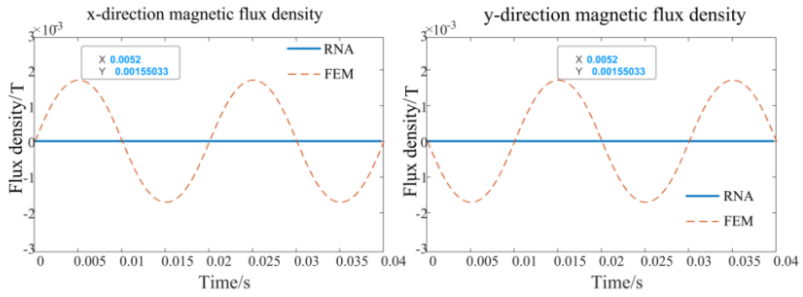

x-direction *y*-direction

(b) Position *c* magnetic flux density waveform at excitation source 25 A

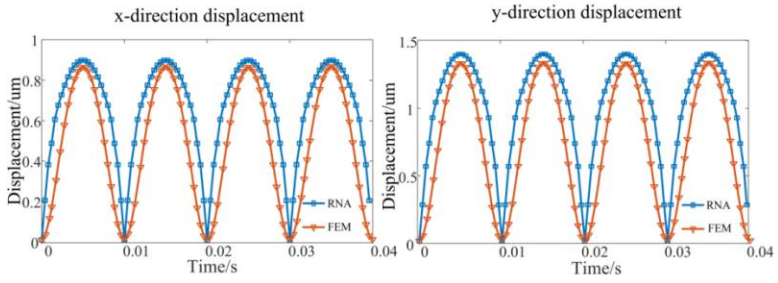

x-direction *y*-direction

(c) Vibration displacement waveform at position *a* during 25 A current excitation

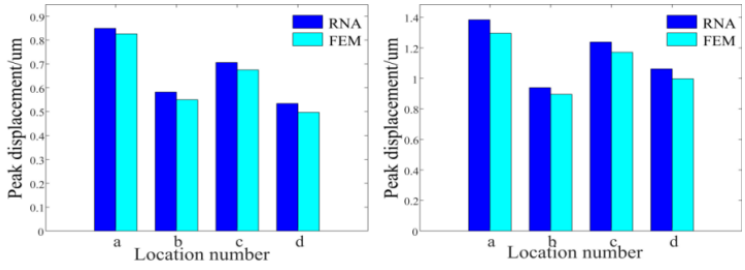

x-direction *y*-direction

(d) Comparison of peak-to-peak vibration displacements at different points under the same current

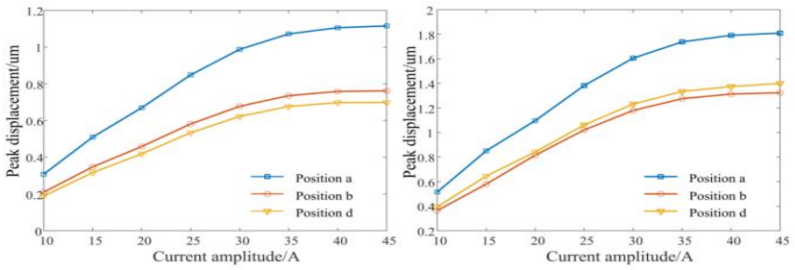

x-direction *y*-direction

(e) Vibration peak-to-peak values for different current excitations

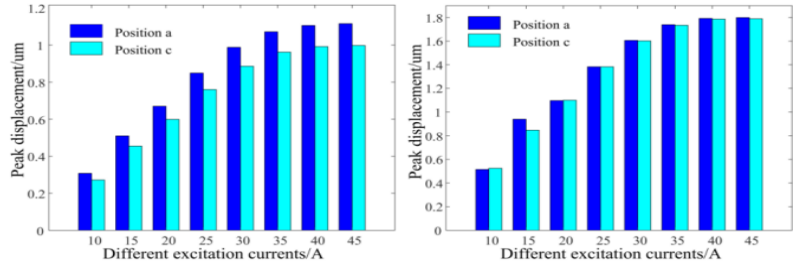

x-direction *y*-direction

(f) Comparison of vibrational displacements at point *a* and point *c* under different currents

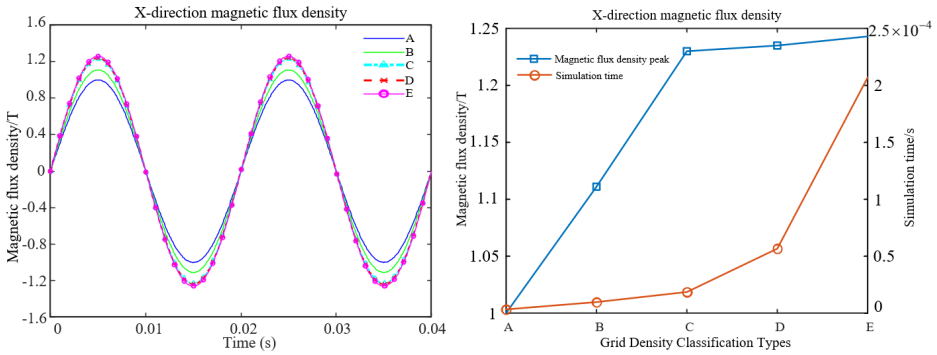

(g) Analysis of convergence for different grids

Fig. 10. Comparison of magnetic flux density and vibration displacement

The core vibration frequency is twice that of the excitation frequency, with the magnitude of vibration proportional to the square of the magnetic flux density, as shown in Fig. 10(c). The distribution of magnetic flux density and vibration amplitude indicates that the finite element calculation results are broadly consistent with measurements taken at similar locations in Reference [23–25], validating the accuracy of this numerical model and computational methodology. The primary reasons for discrepancies in displacement magnitude include the magnetostrictive characteristic curve employed in the calculations and the inability to precisely align computational and measured data points. Nevertheless, the orders of magnitude remain comparable.

Table 2. Specific parameters for different grid types

Grid density degree	Number of grids	Maximum unit size/mm	Minimum unit size/mm
A (highly coarse mesh)	12 537	105	22
B (commom mesh)	17 567	82.5	15.4
C (fine mesh)	31 350	55	9.9
D (relatively fine mesh)	64 682	44	5.5
E (extremely fine mesh)	153 132	30.3	2.2

A convergence study was conducted on the COMSOL model established in this paper to estimate the optimal number of elements required for simulation, as shown in Fig. 10(e). From the coarsest mesh (14 275 elements) to the finest mesh (153 132 elements), the time-dependent variation of the magnetic flux density in the x-direction at point c over 10 simulation cycles (0.2 s) was plotted to determine the optimal mesh size. From Fig. 10(e), we conclude that the results are converged for meshes exceeding 31 350 elements (C). Ultimately, considering both simulation efficiency and accuracy, the simulation employs a mesh comprising 31 350 elements.

3.3. Simulation time comparison

The computer processor of this computing platform is Intel(R) Core i7 @ 1.90 GHz quad-core, and the computer memory is 16 GB. Table 3 gives the magnetic network model and the finite element model to calculate the vibration displacement time comparison analysis It can be seen that the magnetic network model calculation greatly shortens the calculation time, and the magnetic network model time increases with the increase in the number of simulation cycles. The simulation time grows slowly, while the finite element software increases the simulation time with the increase in the number of simulation cycles. The simulation time grows rapidly, and the comparative analysis reflects the advantages of the magnetic network model.

Table 3. Comparison of time-consuming for RNA and FEM to calculate the number of different cycles

Epstein frame		RNA calculation time/s	FEM calculation time/s
Number of simulation cycles (0.02 s/each)	2	3	342
	10	4	1851
	50	5	4213
	100	5	8457

4. Result analysis

In this paper, the four-node reluctance network model is used to calculate the magnetostrictive vibration displacement of the Epstein frame core. The comparison of the results shows the following conclusions:

1. The four-node reluctance network model is suitable for the calculation of the vibration displacement of the core of the electromagnetic equipment. Compared with the widely used finite element calculation method, it can greatly reduce calculation cost, shorten calculation time, and ensure the accuracy of the calculation results in a certain program.
2. In terms of calculation accuracy, the calculation results of the four-node reluctance network model are compared with COMSOL, and the errors are less than 8%, which verifies the rationality of the proposed model. In terms of calculation efficiency, with the increase in the number of simulation cycles, the advantage of shortening the calculation time will be more obvious. When simulating 2 cycles, COMSOL takes about 100 times as much time as the four-node reluctance network model. When simulating 50 cycles, the gap is expanded to 1 000 times, and the efficiency advantage becomes more and more significant with the increase in the simulation cycle.
3. The vibration displacement in the corner area caused by the magnetostrictive effect is significantly greater than that in other parts of the iron core, and the displacement at different positions in the corner area is also different. If the top two points of the inner and outer corners of the corner are significantly larger than other areas of the corner, and the displacement at the inner corner vertex is greater than that at the outer corner vertex in the corner area. So, when designing electromagnetic equipment, the focus should be on vibration reduction and noise reduction at the corners.

Acknowledgements

We thank for the funding from the National Natural Science Foundation of China (52167013) and the Key Project of Gansu Provincial Natural Science Foundation (24JRRA244).

References

[1] Gepend W.W.J., *Analysis and control research on core vibration of UHV shunt reactor [J]*, Transactions of China Electrotechnical Society, vol. 37, no. 9, pp. 2190–2198 (2022), DOI: 10.19595/j.cnki.1000-6753.tces.211477.

[2] Moses A.J.A.P.I., Phophongviwat T., *Contribution of magnetostriction to transformer noise*, Proceedings of the 45th International Universities Power Engineering Conference UPEC2010 IEEE (2010).

[3] Kubiak W.W.P., *Vibration analysis of small power transformer [J]*, COMPEL-The International Journal for Computation Mathematics in Electrical Electronic Engineering, vol. 29, no. 4, pp. 1116–1124 (2010), DOI: 10.1108/03321641011044532.

[4] Xiaojun Z.L.Z., Yang L., *Experimental study on the effect of mechanical stress on the comprehensive magnetic properties of the grain-oriented silicon stee [J]*, Transactions of China Electrotechnical Society, vol. 37, no. 22, pp. 5776–5787 (2022), DOI: 10.19595/j.cnki.1000-6753.tces.210703.

[5] Shahaj A.G.S.D., *A possible method for magnetostrictive reduction of vibration in large electrical machines [J]*, IEEE Transactions on Magnetics, vol. 47, no. 2, pp. 374–385 (2010), DOI: 10.1109/TMAG.2010.2095875.

[6] Bartoletti C.D.M., Di Carlo D., *Vibro-acoustic techniques to diagnose power transformers [J]*, IEEE Transactions on power Delivery, vol. 19, no. 1, pp. 221–229 (2004), DOI: 10.1109/TPWRD.2003.820177.

[7] Datta S., Atulasimha J., Mudivarthi C. *et al.*, *Modeling of magnetomechanical actuators in laminated structures [J]*, Journal of Intelligent Material Systems and Structures, vol. 20, no. 9, pp. 1121–1135 (2009), DOI: 10.1177/1045389X09104262.

[8] Kannan K., Dasgupta A., *A nonlinear Galerkin finite-element theory for modeling magnetostrictive smart structures [J]*, Smart Materials and Structures, vol. 6, no. 3, 341 (1997), DOI: 10.1088/0964-1726/6/3/011.

[9] Wahi S.K., Gupta D., Santapuri S., *Finite element analysis and design of a magnetostrictive material based vibration energy harvester with a magnetic flux path [J]*, Smart Materials and Structures, vol. 33, no. 11, 115038 (2024), DOI: 10.1088/1361-665X/ad8408.

[10] Yanli Z.X.S., Dexin X., *Measurement and simulation of magnetostrictive properties for non-grain oriented electrical steel sheet [J]*, Transactions of China Electrotechnical Society, vol. 28, vol. 11, pp. 176–181 (2013), DOI: 10.19595/j.cnki.1000-6753.tces.2013.11.024.

[11] Yanli Z.X.S., Dexin X., *Modeling of anisotropic magnetostriction property of non-oriented silicon steel sheet [J]*, Proceedings of the CSEE, vol. 34, no. 27, pp. 4731–4736 (2014), DOI: 10.13334/j.0258-8013.pcsee.2014.27.021.

[12] Zhu L.Y.Q., Yan N.R., *Research on vibration and noise of power transformer cores including magnetostriction effects [J]*, Transactions of China Electrotechnical Society, vol. 28, no. 4, pp. 1–6+19 (2013), DOI: 10.19595/j.cnki.1000-6753.tces.2013.04.001.

[13] Kitakawa W.I.Y., Todakat T., *Analysis of structural deformation and vibration of a transformer core by using magnetic property of magnetostriction [J]*, Electrical Engineering in Japan, vol. 172, no. 1, pp. 19–26 (2010), DOI: 10.1002/eej.20947.

[14] Yang I.J.L.S.H., Lee K.B., *A process to reduce the electromagnetic vibration by reducing the spatial harmonics of air gap magnetic flux density [J]*, IEEE Transactions on Magnetics, vol. 57, no. 2, pp. 1–6 (2020), DOI: 10.1109/TMAG.2020.3022844.

[15] Lambert M., *Transformer modeling for low-and mid-frequency electromagnetic transients simulation [D]*, École Polytechnique de Montréal (2014).

[16] Fu D., *Research on modeling and optimization design of new transverse flux permanent magnet linear motor [D]*, Shandong University (2019).

[17] Changjin Z.Z.C., Qingxiao M.E.I. *et al.*, *Nonlinear dynamic equivalent magnetic network model analysis of transverse flux permanent magnet synchronous motor [J]*, Proc. CSEE, vol. 39, no. 1, pp. 307–314+345 (2019), DOI: 10.13334/j.0258-8013.pcsee.180495.

[18] Keman Lin N.L., *Magnetic Circuit Modeling and Characteristics of a New Magnetron Adjustable Reactor Considering Leakage Effect [J]*, Transactions of China Electrotechnical Society, vol. 30, no. 2, pp. 114–121 (2015), DOI: 10.19595/j.cnki.1000-6753.tces.2015.02.015.

[19] Xie W.W.G., LI H., *Equivalent magnetic network model and parameter calculation of separable transformer [J]*, Journal of Harbin Engineering University, vol. 30, no. 7, pp. 747–750 (2009), DOI: 10.3969/j.issn.1006-7043.2009.07.005.

[20] Hane Y., Nakamura K., Kurita N., *A Consideration of Magnetostriction Force Calculation for Transformer Core by Using Reluctance Network Analysis [J]*, Journal of the Magnetics Society of Japan, vol. 45, no. 3, pp. 56–60 (2021).

[21] Du Y., *Research on transformer core vibration based on magnetic-elastic coupling theory [D]*, North China Electric Power University (2020).

[22] Lihua Z., *Study of Affection from Magnetostriction in Laminated Core on Vibration Noise of Transformer and AC Motor [D]*, Hebei University of Technology, Tianjin (2013).

[23] Zhao X., Du Y., Liu Y. *et al.*, *Analysis of DC biased vibration characteristics of iron core using frequency domain method of magnetic mechanical coupling field [J]*, High Voltage Technology, vol. 46, no. 4, pp. 1216–1225 (2020), DOI: 10.13336/j.1003-6520.hve.20200430013.

[24] Zhao X., Zhang J., Wang H. *et al*., *Fine tuned simulation method for transformer iron core vibration characteristics considering the influence of air gap from the perspective of electric magnetic mechanical coupling [J]*, Transaction of China Electrotechnical Society, vol. 39, no. 14, pp. 4257–4269 (2024), DOI: 10.19595/j.cnki.1000-6753.tces.230719.

[25] Kitagawa W., Ishihara Y., Todaka T. *et al.*, *Analysis of structural deformation and vibration of a transformer core by using magnetic property of magnetostriction [J]*, Electrical Engineering in Japan, vol. 172, no. 1, pp. 19–26 (2010).